A Time Series Weather Radar Simulator Based on High-Resolution Atmospheric Models

B. L. CHEONG AND R. D. PALMER

School of Meteorology, University of Oklahoma, Norman, Oklahoma

M. XUE

School of Meteorology, and Center for Analysis and Prediction of Storms, University of Oklahoma, Norman, Oklahoma

(Manuscript received 28 September 2006, in final form 8 March 2007)

ABSTRACT

A three-dimensional radar simulator capable of generating simulated raw time series data for a weather radar has been designed and implemented. The characteristics of the radar signals (amplitude, phase) are derived from the atmospheric fields from a high-resolution numerical weather model, although actual measured fields could be used. A field of thousands of scatterers is populated within the field of view of the virtual radar. Reflectivity characteristics of the targets are determined from well-known parameterization schemes. Doppler characteristics are derived by forcing the discrete scatterers to move with the three-dimensional wind field. Conventional moment-generating radar simulators use atmospheric conditions and a set of weighting functions to produce theoretical moment maps, which allow for the study of radar characteristics and limitations given particular configurations. In contrast to these radar simulators, the algorithm presented here is capable of producing sample-to-sample time series data that are collected by a radar system of virtually any design. Thus, this new radar simulator allows for the test and analysis of advanced topics, such as phased array antennas, clutter mitigation schemes, waveform design studies, and spectral-based methods. Limited examples exemplifying the usefulness and flexibility of the simulator will be provided.

1. Introduction

A realistic numerical simulation can provide a deterministic and controlled environment for a wide variety of engineering and scientific studies. Extreme scenarios can be simulated to test the robustness and limitations of signal-processing techniques, which help identify and scrutinize factors that may have been overlooked during the development process. Weather radar–like signals have been simulated since at least the 1970s. For example, work by Zrnić (1975) was based on an assumed, but arbitrary, Doppler spectral form. The inverse Fourier transform of this spectrum was performed to produce time series data corresponding to that spectral shape. Numerous statistical studies were made possible using this simulation. Based on the algorithm by Zrnić (1975), Chandrasekar and Bringi (1987) developed a simulation scheme to generate radar reflectivity for a simulated raindrop size distribution that had a gamma distribution (Ulbrich 1983). In that work, the simulation was used to investigate the correlation of radar estimates and rainfall rate.

To devise a more realistic time series simulator, Capsoni and D'Amico (1998) formulated a physically based procedure to simulate pulse-to-pulse time series by coherently summing all the returns from individual hydrometeors within a resolution volume, assuming a gamma raindrop size distribution. Characteristics of the radar, such as range weighting and antenna beampattern weighting within the main lobe and the adjacent two sidelobes, were considered. Given the computational complexity, however, the process was limited to generation of time series data within a single range gate. This work was followed by an algorithm for simulating dual-polarization time series data (Capsoni et al. 2001) in which the effects of hydrometeors with different shapes and sizes were taken into account.

Corresponding author address: Dr. Boon Leng Cheong, School of Meteorology, University of Oklahoma, 120 David L. Boren Blvd., Suite 5900, Norman, OK 73072.
E-mail: boonleng@ou.edu

DOI: 10.1175/2007JTECHA923.1

For numerous applications, it is often not necessary to generate time series data when realistic moment maps would suffice. For example, Krajewski et al. (1993) used a simulation scheme to generate radar-estimated rainfall fields without simulating time series data. Radar measurements, that is, reflectivity and differential reflectivity, were directly derived from a two-dimensional stochastic space–time model of rainfall events and drop size distribution. These radar-derived measurements were then used to estimate rainfall rate. Anagnostou and Krajewski (1997) presented a similar simulation procedure, with the addition of vertical structure making a true three-dimensional model. The antenna beam pattern within the 3-dB beamwidth of the main lobe was considered in the process of generating the radar-estimated field.

Recently, May et al. (2007) developed a radar moment simulator using output from a physically modeled three-dimensional volume that is characterized by multiple atmospheric fields. The simulated atmospheric volume was generated from the high-resolution numerical weather simulations using the Advanced Regional Prediction System (ARPS; Xue et al. 2000, 2001), in which the microphysical species including the rainwater content is parameterized with a Marshall–Palmer drop size distribution (Marshall and Palmer 1948). Similar to Capsoni et al. (2001), range and antenna weighting were considered. However, May et al. (2007) simulated a full three-dimensional volume, although just for spectral moments. Atmospheric effects such as anomalous propagation and attenuation through rain were investigated in detail. This simulator provides a powerful tool for the design and optimization of radar experiments under realistic atmospheric scenarios. Another recent example of a radar simulator based on atmospheric model output is the work of Caumont et al. (2006). This simulator was designed to be an integral part of the high-resolution Meso-NH model and has been used for sensitivity studies with the goal of the optimization of reflectivity assimilation. As such, the simulator was not designed with either Doppler or polarimetric capabilities.

In the present work, the development of a radar simulator, capable of generating realistic, three-dimensional, time series data, is presented. The simulator uses a Lagrangian framework with thousands of scatterers moving with the wind field produced from a high-resolution atmospheric numerical model. The motion of the targets causes variations in radar phase producing a Doppler shift. The radar signals are generated by appropriately weighted integration of all targets within the resolution volume of the radar. A full three-dimensional view is possible by scanning this volume to any desired location. This Lagrangian approach was inspired by the work of Holdsworth and Reid (1995) in which radar time series for a very high frequency (VHF) wind profiler was generated using hundreds of discrete point scatterers. Recent work by Cheong et al. (2004a) illustrated a more efficient and flexible approach to incorporate realistic atmospheric parameters into the simulator. In that work, a table lookup and four-dimensional linear interpolation approach were used to extract and infuse a set of pregenerated atmospheric parameters into the process of generating time series data. A similar approach is adopted here but for the case of side-looking weather radars instead of a profiler.

The next section provides the overall structure of the radar simulator in addition to an overview of the numerical weather prediction model used. Useful comments on the use of interpolation and the proposed table lookup procedures are outlined in section 3. Examples using the simulator for two distinct radar configurations are provided in section 4. Finally, conclusions drawn from this research are given in the last section.

2. Algorithmic structure of the radar simulator

The proposed simulator produces time series samples of a radar by coherently adding thousands of discrete signals from a simulation domain. Each discrete signal represents a reflection from a point scatterer, which is an amplitude-attenuated and phase-shifted replica of the transmitted pulse. In this simulator, the primary goal is to derive realistic radar returns given an arbitrary but known reflectivity field from the atmospheric model ARPS. The reflectivity factor of each point scatterer is set to be a function of its position within the simulation domain while the phase is a function of its two-way path distance relative to the radar.

a. Overview of simulated atmospheric fields

The model-simulated dataset used to test our radar simulator was produced by the ARPS model (Xue et al. 2000, 2001), which was also used by May et al. (2007). The simulation used here has twice as much horizontal resolution, however. The ARPS is a fully compressible and nonhydrostatic prediction model and its prognostic state variables include wind components u, v, w, potential temperature θ, pressure p, the mixing ratios for water vapor q_v, cloud water q_c, rainwater q_r, cloud ice q_i, snow q_s, and hail q_h, plus the turbulent kinetic energy used by the 1.5-order subgrid-scale turbulent closure scheme (see Xue et al. 2000, 2001, 2003 for details).

For the current simulation, only the Kessler-type warm-rain microphysics is used. The simulation had a horizontal grid spacing of 25 m over a 48 km × 48 km domain during the period of time that data are used here, and the vertical grid is stretched and has a vertical spacing of 20 m at the surface. The simulation was for a tornadic supercell thunderstorm, and the storm was initiated by a thermal bubble in a horizontally homogeneous environment defined by the 20 May 1977 Del City, Oklahoma, sounding reported in Ray et al. (1981).

For the ARPS simulation, a horizontal resolution of 50 m was first used and the entire simulation length was over 4 h. An intense tornado developed after 3.5 h into the simulation on the 50-m grid. Over a half-hour period centering on the time of the most intense tornado, a simulation using a 25-m resolution is performed, starting from an initial condition interpolated from the 50-m grid. On this grid, an F4–F5 intensity tornado with a maximum ground-relative wind speed of over 120 m s^{-1} was obtained, with a pressure drop of over 80 hPa at the center of the tornado vortex. The simulated tornado vortex is about 200 m in diameter near the ground. Because of the small size and great intensity of the tornado vortex, spatial and temporal variabilities associated with the tornado are extreme. Gridded outputs with all model fields are available at 1-s intervals from this simulation. Detailed analysis of the simulated tornado is not very important here and will be reported elsewhere.

In Xue et al. (2007), a single time output from the same 25-m simulation near the time of most intense tornado was sampled by a simple Gaussian beam-pattern-based radar simulator to create simulated radial velocity data for testing a variational velocity analysis scheme combined with azimuthal oversampling. Liu et al. (2007) further used the dataset to test a wavelet-based tornado detection algorithm.

In the proposed time series simulator, at any given instance in time, we will use two time level outputs from this 25-m model simulation as input to our radar emulator to create simulated observations.

b. *Spatial/temporal evolution of scatterers*

The radar echo from a transmitted pulse is a complex function of continuous fields of reflectivity and velocity, which depend on the true atmospheric conditions and are thus impractical for analytical solution. However, it is possible to approximate this function by using a large number of discrete scatterers that are randomly distributed over the domain of interest. This is essentially a spatial sampling problem and the composite signal is obtained by coherently integrating the reflected signals from each discrete scatterer. Compared to the volume-scattering case, the returned signal from a single discrete scatterer is much simpler and analytical solutions exist. Volume scattering is approximated by summing the returned echoes from tens of thousands of discrete scatterers that exist within the field of view of the radar. This process is termed *Monte Carlo integration* (Metropolis and Ulam 1949).

The coherently integrated signal from of all the discrete scatterers is referred to as the composite signal. Each sample of the composite signal is a complex sum of the baseband signal from all the individual scatterers, which can be expressed mathematically as follows:

$$x = \sum_{k=0}^{N-1} A^{(k)} \exp[-j\psi^{(k)}] + \mathcal{N}, \tag{1}$$

where superscript $(\cdot)^{(k)}$ indicates the index of the discrete scatterers, N is the total number of scatterers, $A^{(k)}$ represents the amplitude of the signal from the kth scatterer, $\psi^{(k)}$ represents the phase of the kth scatterer, and $\mathcal{N}$ represents additive white Gaussian noise signal. Equation (1) is the general form for producing the composite signal and can be readily extended to simulate systems that use multiple receivers, multiple frequencies, and/or multiple pulse repetition times (PRTs), for example.

Figure 1 is an artist's depiction of the general structure of the proposed weather radar simulator algorithm. To initialize the simulator, an enclosing volume is defined that includes the radar's field of view plus a small margin to mitigate undesirable effects caused at the fringes of the volume. A set of scatterers (typically thousands) is randomly positioned within this enclosing volume, with a uniform distribution. At each sample time (PRT), the composite returned signal is derived using Eq. (1). As time progresses, the position of each discrete scatterer is updated based on its velocity and PRT. There are two components in updating and replacing the scatterers. First, scatterers that exit the enclosing volume (due to the position update) are replaced with randomly positioned new scatterers. It should be emphasized here that in order to properly emulate the composite signal using Monte Carlo integration, the spatial uniformity of the scatterer distribution must be maintained. Second, in order to avoid the scenario in which convergent (or divergent) flows cluster together (or spread apart) the scatterers, it was necessary to implement a random replacement routine. Clearly, this strategy depends on the wind field structure. For example, for radar simulations from a vertically pointing radar, with dominant transverse wind (horizontal), such a routine would not be necessary

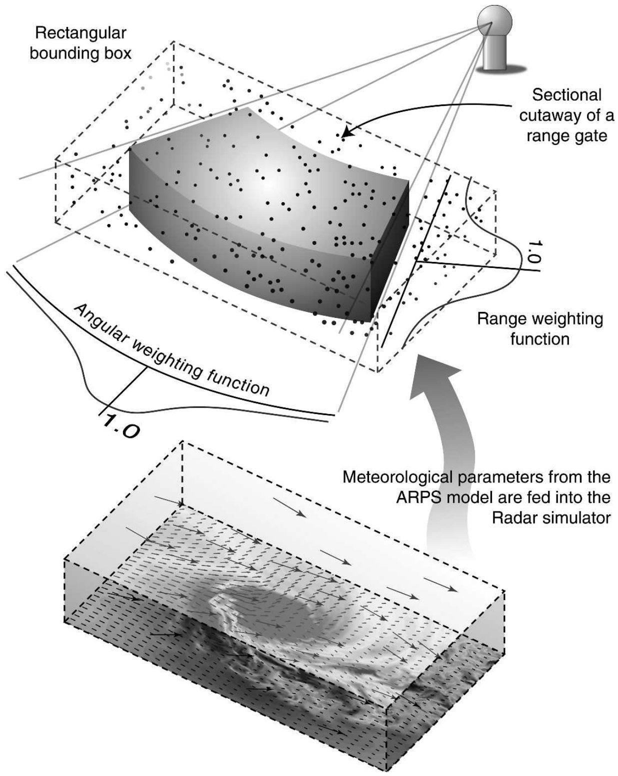

FIG. 1. Conceptual diagram of the time series radar simulator. Each point scatterer represents a discrete position from which the transmit pulse is reflected. Meteorological parameters from the ARPS model are used to derive the reflectivity and velocity of each discrete scatterer. All reflected echoes are integrated to obtain the composite returned signal. As the number of points increases, the composite returned signal approximates well that which would be expected from volume scattering.

(Holdsworth and Reid 1995; Yu et al. 2000). In our case, however, random replacement was needed given the flows present in the storm simulation fields. Randomly replacing scatterers at each sampling time, such that all targets are replaced every 5 s, provides satisfactory results. This process is equivalent to considering that each discrete scatterer has a limited lifetime.

The positions of each scatterer are updated with the instantaneous velocity field and a random component that relates to subgrid turbulent kinetic energy (TKE). The velocity and TKE fields are extracted and interpolated from a set of pregenerated fields, which will be discussed later. The position update can be mathematically described as follows:

$$\mathbf{X}^{(k)}(n) = \mathbf{X}^{(k)}(n-1) + \mathbf{V}^{(k)}(n-1)T_s, \tag{2}$$

where $\mathbf{X}^{(k)}(n) = [x\ y\ z]$ represents the position vector of the kth scatterer at time n, and $\mathbf{V}^{(k)} = [\tilde{u}\ \tilde{v}\ \tilde{w}]$ represents the velocity vector of the kth scatterer and T_s represents the sampling interval, that is, the PRT of the radar system.

As mentioned previously, each velocity component is obtained from the wind velocity and subgrid TKE fields. They are described as follows:

$$\tilde{u} = u + \epsilon\sqrt{\frac{2}{3}\mathrm{TKE}}, \tag{3}$$

$$\tilde{v} = v + \epsilon\sqrt{\frac{2}{3}\mathrm{TKE}}, \tag{4}$$

$$\tilde{w} = w + \epsilon\sqrt{\frac{2}{3}\mathrm{TKE}}, \tag{5}$$

where the second term of Eqs. (3), (4), and (5) represents an instantaneous perturbation of velocity vectors due to the subgrid TKE. It is obtained by scaling the output of a random number generator ϵ that has a normal distribution and unity variance.

In Eq. (1), the phase of the backscattered signal from each discrete scatterer depends on the number of cycles the signal has gone through during its travel from the radar to the target and back to the radar. To be more precise, the phase is also a function of backscattered complex amplitude of each particle, but this complication is not necessary to realistically simulate the radial velocity of the scatterer. In other words, we want to produce time series data that carry the signatures of a Doppler spectrum that is representative of the wind field distributions from the ARPS model. Thus, only the phase change from pulse to pulse is needed and not the phase due to the scatterer. The phase is given by the following equation:

$$\psi^{(k)} = \frac{2\pi D^{(k)}}{\lambda}, \tag{6}$$

where $D^{(k)}$ represents the *two-way* distance of the kth scatterer and λ represents the wavelength of the radar system. It is easily justified to assume that the initial phase of the transmit signal is zero. The Doppler shift of each target is created by the change of phase with time, which is controlled by the position update Eq. (2).

In the following sections, the important amplitude term in Eq. (1) will be discussed. The spatial weighting functions (range and angle), used in the Monte Carlo integration process, will first be presented. Then, the reflectivity parameterization scheme will be provided.

c. *Weighting functions*

Ignoring system losses, the amplitude of the kth scatterer $A^{(k)}$ depends on the transmit power, antenna pattern, range weighting function, reflectivity, and range.

The weighting functions (angle and range) account for the varied contribution from each scatterer at a specific angle and range. The reflectivity of each scatterer is a function of atmospheric conditions, which is derived from realistic physical parameters, and will be described in the next section. Radar parameters that are shared among all discrete scatterers, such as transmit power and antenna gain, are set constant. Given the perfect calibration possible with simulations, these common parameters are considered relatively unimportant in the process of computing the amplitude. The amplitude for a scatterer at an arbitrary location (x, y, z) can be described as

$$A(x, y, z) = \left(\frac{1}{r^4} w_a w_r Z_e\right)^{(1/2)}, \tag{7}$$

where r represents the range of the scatterer from the radar, w_a is the angular weighting function of the two-way beam pattern, w_r is the range weighting function, and Z_e represents the parameterized equivalent reflectivity factor. For notational convenience, the dependence of w_a, w_r, and Z on position (x, y, z) is not explicitly stated but is assumed throughout this paper. It should be emphasized that the backscattered power is inversely proportional to r^4 since point targets are used in the simulator. Through the Monte Carlo integration process, however, the range dependence will be reduced to r^2 given the volume integration performed.

The range weighting function, shown in Fig. 1, simulates the effect of pulse shape and receiver filtering on each scatterer. Scatterers near the center of the range gate and near the boresight of the radar will have the maximum weighting. For a narrowband receiver with a time–bandwidth product equal to unity, the (power) range weighting function can be sufficiently approximated with a Gaussian function centered around the desired range r_0 and is given by Doviak and Zrnić (1993):

$$w_r = \exp\left[-\frac{(r - r_0)^2}{2\sigma_r^2}\right], \tag{8}$$

where $\sigma_r = 0.35\Delta r$ in which Δr represents the range resolution given by

$$\Delta r = \frac{c\tau}{2}. \tag{9}$$

The speed of light is denoted by c (3×10^8 m s^{-1}) and τ is the pulse duration.

For a typical parabolic dish antenna, the normalized *one-way* transmit beam pattern has a sine functionality with the largest gain concentrated on the main lobe of the pattern. This function is well approximated by the following equation (Doviak and Zrnić 1993):

$$w_{tx}(\varphi) = \left\{\frac{8J_2[(\pi D \sin\varphi)/\lambda]}{[(\pi D \sin\varphi)/\lambda]^2}\right\}^2. \tag{10}$$

The angular distance from the beam axis (boresight) is given by φ and J_2 is the Bessel function of the first kind (second order). For a monostatic radar system that uses the same antenna for transmit and receive, the power-normalized *two-way* beam pattern is simply the square of Eq. (10), given by

$$w_a(\varphi) = w_{\mathrm{tx}}(\varphi) w_{\mathrm{rx}}(\varphi), \tag{11}$$

where w_{tx} and w_{rx} would be equal, in this case. For more advanced applications, such as phased array antennas and imaging radars, the simulator has been designed to allow for the case of different transmit and receive beam patterns. Examples from each case will be presented in section 4.

d. Parameterization of reflectivity

The fundamental control of each discrete scatterer is governed by the ARPS-generated atmospheric fields. However, reflectivity factor in Eq. (7) is not a standard output parameter of the ARPS model and must therefore be calculated from known model microphysical parameters. Based on the work of Smith et al. (1975) and for the purpose of radar data assimilation, Tong and Xue (2005) developed the scheme that is used here to characterize the equivalent reflectivity factor of the individual scatterers under the Rayleigh assumption. In that work, the total equivalent reflectivity factor was given by

$$Z_e = Z_r + Z_s + Z_h, \tag{12}$$

where Z_r, Z_s, and Z_h represent the reflectivity factors from the three precipitating hydrometeors, that is, the rainwater, snow, and hail, respectively. Of course, it is more standard to present reflectivity factor in units of dBZ, which can be calculated using the following equation:

$$Z_{\mathrm{dB}Z} = 10 \log_{10}\left(\frac{Z_e}{1\ \mathrm{mm}^6\ \mathrm{m}^{-3}}\right). \tag{13}$$

In the work of Tong and Xue (2005), the rainwater component of the equivalent reflectivity factor was determined to have the following form:

$$Z_r = \frac{10^{18} \times 720(\rho q_r)^{1.75}}{\pi^{1.75} N_r^{0.75} \rho_r^{1.75}}, \tag{14}$$

where ρ is the air density (kg m^{-3}), q_r is the rainwater mixing ratio (kg kg^{-1}), and $N_r = 8.0 \times 10^6$ m^{-1} is the

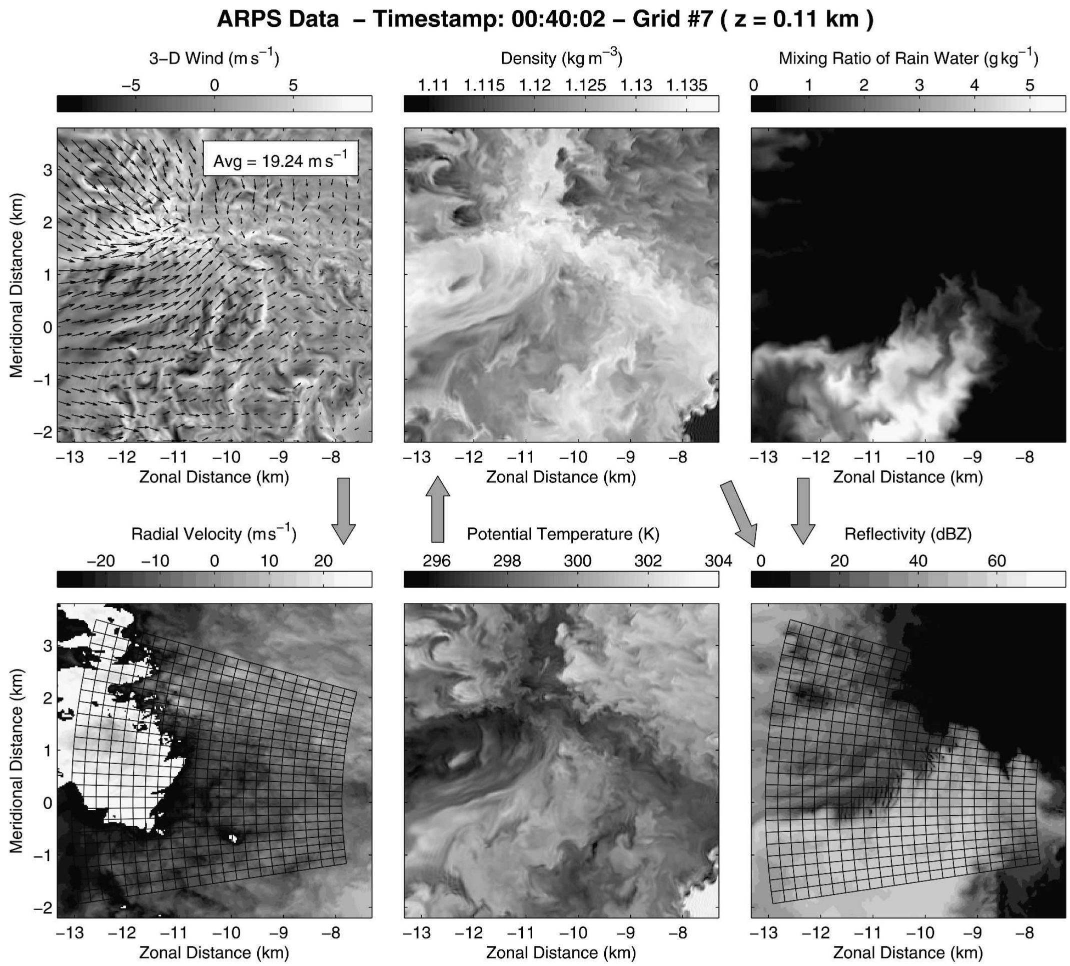

FIG. 2. Example snapshot of the ARPS atmospheric fields at 0.11 km above ground level. The three-dimensional wind 1), pressure, potential temperature, and hydrometeor mixing ratio fields are readily available as standard outputs of ARPS. The latter three are used to derive the equivalent reflectivity factor according to Eq. (12), and the reflectivity (dBZ) is displayed in the lower-right panel. The grid lines in the radial velocity and reflectivity panels show the sampling volumes of the simulations to be discussed in the next section.

intercept parameter in the assumed Marshall–Palmer exponential raindrop size distribution. Regions with snow have possible contributions to Z_e from both dry and wet snow. In such cases, a 0°C threshold in air temperature is used to distinguish the respective contributions. This component of the total equivalent reflectivity factor due to snow has been shown to have the following form (Tong and Xue 2005):

$$Z_s = \begin{cases} \dfrac{10^{18} \times 720|K_i|^2 \rho_s^{0.25} (\rho q_s)^{1.75}}{\pi^{1.75} |K_r|^2 N_s^{0.75} \rho_i^2} & T \leq 0°\text{C} \\ \dfrac{10^{18} \times 720 (\rho q_s)^{1.75}}{\pi^{1.75} N_s^{0.75} \rho_s^{1.75}} & T > 0°\text{C}, \end{cases} \tag{15}$$

where $\rho_s = 100$ kg m^{-3} is the density of snow, $\rho_i = 917$ kg m^{-3} is the density of ice, $N_s = 3.0 \times 10^6$ m^{-4} is the intercept parameter for snow, $|K_i|^2 = 0.176$ is the dielectric factor for ice, and $|K_r|^2 = 0.93$ is the dielectric factor for water. Finally, for the case of hail, the wet hail formation is used and given by Smith et al. (1975):

$$Z_h = \left(\frac{10^{18} \times 720}{\pi^{1.75} N_h^{0.75} \rho_h^{1.75}} \right)^{0.95}, \tag{16}$$

where $\rho_h = 913$ kg m^{-3} is the density of hail, and $N_h = 4.0 \times 10^4$ m^{-4} is the intercept parameter of hail.

Given the atmospheric fields generated by the ARPS model and the scheme for calculating the equivalent reflectivity factor, it is now possible to produce the needed fields for the radar simulator. An example of the ARPS fields from the 25-m tornadic thunderstorm simulation is provided in Fig. 2. The upper three panels (from left to right) provide the wind fields (horizontal

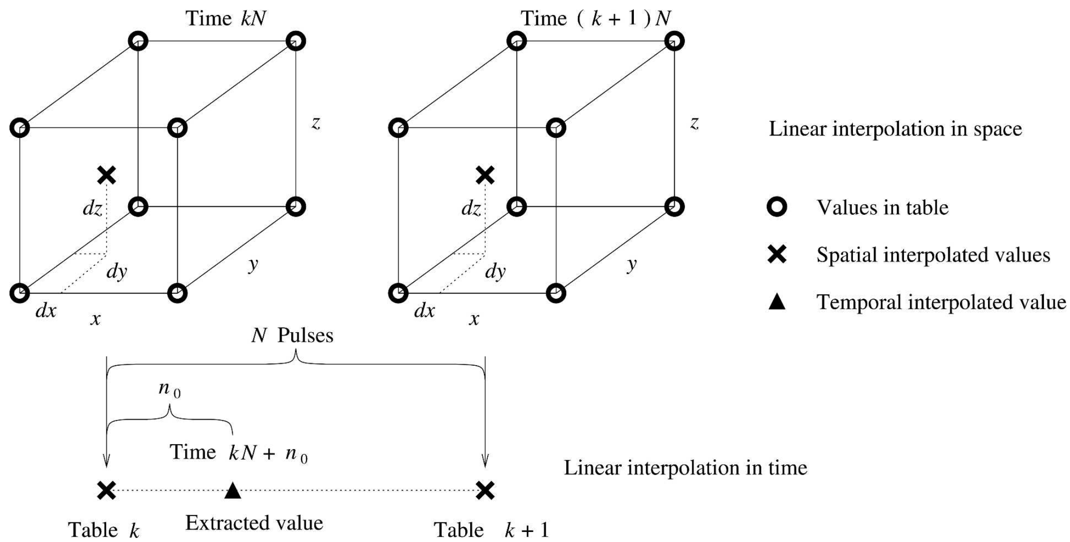

FIG. 3. Table lookup and quad-linear interpolation procedure. At time (kN+n_0), two values in space are obtained via trilinear interpolation from table k and (k + 1). Following this calculation, the resulting two values are linearly interpolated in time to obtain the final value (adapted from Cheong et al. 2004a).

wind vectors plus vertical velocity in shades), air density, and rainwater mixing ratio, respectively. Assuming a simulated radar position to the right of the displayed fields, the radial velocity (Fig. 2d) is derived from the three-dimensional wind by simple projection. The potential temperature is shown in Fig 2e. Equivalent reflectivity factor derived from the ARPS fields is shown in Fig. 2f. Note that even though our reflectivity simulation can handle the effect of ice species, our current dataset does not contain ice. As expected, regions of high Z_e follow regions with high rainwater mixing ratio. These fields are used in Eq. (1) to produce time series data. Therefore, we will consider the data in Fig. 2 as ground truth, with the resolution provided by the inherent grid spacing of the ARPS output.

3. Quad-linear spatial and temporal interpolation

The atmospheric fields, which control the flow and dictate the characteristics of the scatterers, are typically generated separately from the actual radar simulation. In other words, the *pregenerated* atmospheric fields do not directly affect the algorithmic flow of the simulation. Given the input fields, it is essential to grid the data with a format that can be readily fed into the simulator. For efficiency, a lookup procedure and linear interpolation are used to extract the atmospheric parameters corresponding to individual discrete scatterers (Cheong et al. 2004a). Using this technique, the simulator has the flexibility to incorporate atmospheric fields previously generated by a variety of models. Therefore, it is not necessary to regenerate the fields for each run of the simulator.

For any instance in time, two three-dimensional grids of atmospheric data, valid at time levels k and $(k + 1)N$ (two time levels are needed for linear interpolation in time), are used to simulate the desired temporal continuity for all model parameters. Figure 3 illustrates the procedure of extracting a parameter for an example of time (kN + n_0) at position (x, y, z). The nearest eight values per time level (denoted by circles in the figure) are extracted from grids at time level k and (k + 1). Subsequently, these two sets of eight values are weighted-and-summed via trilinear interpolation in space to produce two values (separated in time) for the position (x, y, z). Finally, these two values are linearly interpolated in time to obtain the parameter value at position (x, y, z) at time (kN + n_0). Obviously, this procedure is a quad-linear interpolation process.

Note that the grid cells of the input model do not have to be rectangular. The upper and lower surfaces of the grid cells do not have to be flat, which is the case of terrain-following computational coordinates, as used by the ARPS and many other atmospheric models. The needed model parameters—for example, q_r—are interpolated to the position and time of the scatterers, and the radar reflectivity is then calculated for individual scatterers.

4. Illustrative examples using the radar simulator

In this section, three examples to demonstrate the flexibility and utility of the proposed simulator are pre-

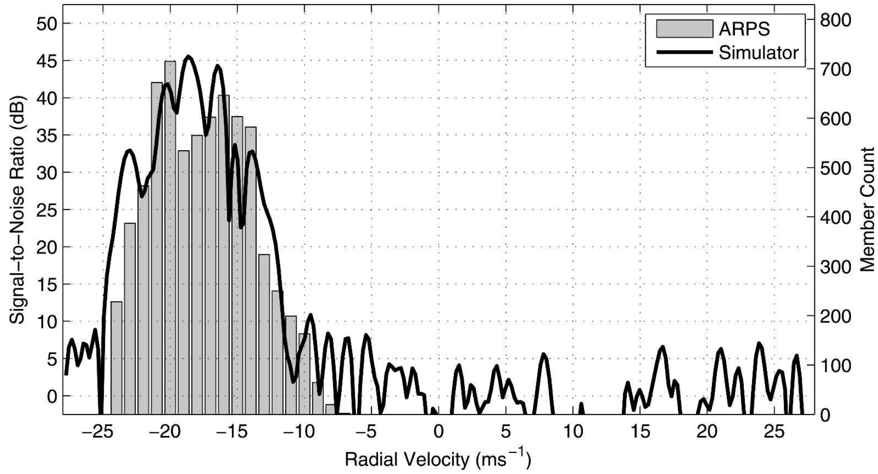

FIG. 4. A histogram of the radial velocities derived from the true wind vectors from the ARPS model and the Doppler spectrum of the time series data from the simulator. Without any spatial variation of reflectivity, the time series is solely modulated by the motion of scatterers due to the atmospheric wind field and can be seen to agree with the distribution of the true wind field, represented by the histogram.

sented. As discussed previously, the radar simulator uses Monte Carlo integration to emulate volume scattering. Because of the inherent sampling process, it is important that the number of scatterers be sufficiently large. By balancing adequate sampling of the desired atmospheric features and computational cost, a general rule has been determined that each simulated resolution volume (gridded region in Fig. 2) should contain at least 20 scatterers.

For a range of r, an approximation of the size of the resolution volume is given by

$$\Delta V \approx r^2(\Delta\theta)(\Delta\phi)(\Delta r), \tag{17}$$

where $\Delta\theta$ and $\Delta\phi$ represent the two angular beamwidths of the antenna in azimuth and elevation, respectively. This approximation will be used later to determine the required number of scatterers for each simulation.

a. Single range gate canonical example

A simple one range gate simulation is presented in this section. To illustrate simulating time series data that are solely modulated by the motions of the atmosphere, we have overridden the reflectivity values from the ARPS model and set them to a constant value for all scatterers. A radar is configured to have a 2° antenna beamwidth and a 1.5-μs pulse width ($\Delta r \approx 225$ m), directed to a volume located 20 km away from the radar. With this configuration, the resultant domain is approximately 700 m × 300 m × 450 m, that is, a domain size that can contain 27 resolution volume cells (one additional cell on each side) in order to effectively represent the contribution from neighboring gates. This simulation domain encompasses more than 7000 grid points from the ARPS model. For this example, 540 discrete scatterers (20 per resolution volume) were used.

Figure 4 shows the histogram of radial velocities derived from the true wind vectors and the Doppler spectrum of the time series data from the simulator. One can see that the simulator correctly produced a time series that has a velocity spectrum that agrees with the wind field being injected into the simulator through the table lookup and interpolation process.

b. Parabolic-dish scanning radar

As a first test of the proposed radar simulator, a mechanically scanned, parabolic-dish radar, which closely mimics the parameters of the Weather Surveillance Radar-1988 Doppler (WSR-88D), was simulated. The operating frequency was set to 2.7 GHz with a symmetric, two-way, 3-dB beamwidth of 0.95°. A pulse of 1.57 μs in length was used, providing 235-m range resolution. An aliasing velocity of 27.8 m s^{-1} resulted from the 1-ms PRT. An elevation angle of 0.5° was used with the first of 22 range gates set at 8 km. The radar was scanned over a 24° swath of the ARPS simulated atmosphere, which contained a tornado producing a hook echo in the reflectivity plots. The subvolume of the model data used for the radar simulator (see Fig. 1) had a size of 6 km × 6 km × 0.24 km. Given that the resolution volume at 10 km (middle of the domain) is approximately 6.46×10^6 m^3, at least 2.67×10^4 scatterers are needed in order to meet the aforementioned condition of 20 scatterers per resolution volume. Therefore, 30 000 discrete scatterers were used for this example. The radar was scanned over the 24° angular region with a 1° azimuthal sampling interval, although finer sampling could easily be achieved. The antenna rotation rate was set to produce 50 samples for each azimuth angle with a 50-ms dwell time. Gaussian-distributed, complex noise was added to the time series data in order to simulate electronic receiver noise. Since the noise floor should be approximately constant for a particular radar system, the additive noise power was chosen to produce an average signal-to-noise ratio (SNR) of 70 dB over the entire domain (azimuth angles and range) scanned by the radar.

Using the 50 time series samples, the autocorrelation function at lags 0, 1, and 2 were estimated for each range gate and azimuth angle. These results were used with covariance processing to produce estimates of reflectivity, radial velocity, and spectrum width, which are shown in the top three panels of Fig. 5. The simulated radar is located to the right of the figure, which determined the orientation of the radial velocity. The limits of plot axes indicate the size of the input data grid or enclosing volume. As can be seen, the enclosing volume is larger than the actual simulated region, which mitigates artifacts caused by boundary effects as scatterers enter/exit the volume (Holdsworth and Reid 1995).

Markers on the moment fields indicate the locations, for which time series and corresponding Doppler spectral estimates are shown at the bottom of the figure. Five examples were chosen to sample a variety of atmospheric conditions. The first example (denoted by a circle) corresponds to an extremely low-SNR case with the expected flat spectral shape. The time series show low-amplitude fluctuations typical of noise-dominated signals. Note that the axis scales for the time series plots are not constant. The next example (denoted by a triangle) has the strongest backscattered power from the set and shows an inbound velocity of approximately -11.78 m s^{-1}. The reflectivity is over 60 dBZ near the core of the mesocyclone as indicated by large dashed circle in upper-left panel. The last three examples provide illustrations of partial aliasing, due to the 27.8 m s^{-1} unambiguous velocity and various reflectivity levels. In general, the estimated Doppler spectra have a shape (Gaussian) that is expected from volume-filled atmospheric scatter, lending credibility to the Monte Carlo integration scheme used.

c. *Phased array imaging radar*

As another example of the utility of the radar simulator, a more advanced radar design is now used. Here, a phased array radar system has been simulated with a transmit frequency of 3.2 GHz, a pulse width of 1.57 μs ($\Delta r = 235$ m), and a PRT of 1 ms. The radar is scanning at an elevation angle of 1.5° at a range of 10 km for the first gate. Twenty-two (22) range gates are used with an 18° azimuthal coverage (0.75° sampling) to observe the cyclonic circulation present in the ARPS data. To test aircraft clutter mitigation using adaptive beam forming and to illustrate the flexibility of the radar simulator, a strong point target (aircraft) has been inserted into the atmospheric fields of the ARPS model, flying toward the northeast within the field of view, at a speed of 28 m s^{-1}. For simplicity, the reflectivity of the aircraft has been chosen to be an arbitrarily high value of 80 dBZ in order to have a target that obscures the weather signals. The enclosing volume for this simulation is approximately 6 km × 5.2 km × 0.5 km.

The simulated radar uses a *spoiled* transmit beam that has a uniform 18° azimuth coverage. In practice, this can be accomplished by either using a subset of transmit elements that is closer to the center of the array, or an independent transmitter that has a wide beam pattern. In elevation, the transmit beam has a beamwidth ($\Delta\theta$) of 1.5° with a Gaussian weighting applied so that scatterers on the scanning elevation plane contribute most significantly. Such a radar design will allow the scanned region to be simultaneously observed from all directions. The 93 receive elements of the array are shown in Fig. 6 and are assumed to be omnidirectional. In this case of an imaging radar, the simulator will produce time series data for each of the receive elements. The azimuthal resolution can be estimated using (Stoica and Moses 1997)

$$\Delta\theta = \sin^{-1}\left(\frac{1}{L}\right), \tag{18}$$

where $L = (m - 1)d/\lambda$ is the array length measured in wavelengths, m is the number of elements across the longest aperture, that is, $m = 31$, and d is the element spacing, which is 10 cm for this particular configuration. The *azimuthal* angular resolution ($\Delta\phi$) is therefore approximately 1.79°. Using a similar procedure to the previous example to calculate the average number of scatterers for the closest range gate and assuming that the elevation weighting limits the resolution volume as $\Delta\phi = 1.5°$, $\Delta V \approx r^2(\Delta\theta)(\Delta\phi)(\Delta r) = 1.92 \times 10^7$ m^3. Therefore, at least 1.62×10^4 discrete scatterers are needed for proper sampling. The number of scatterers was set to 20 000 to provide some margin of error.

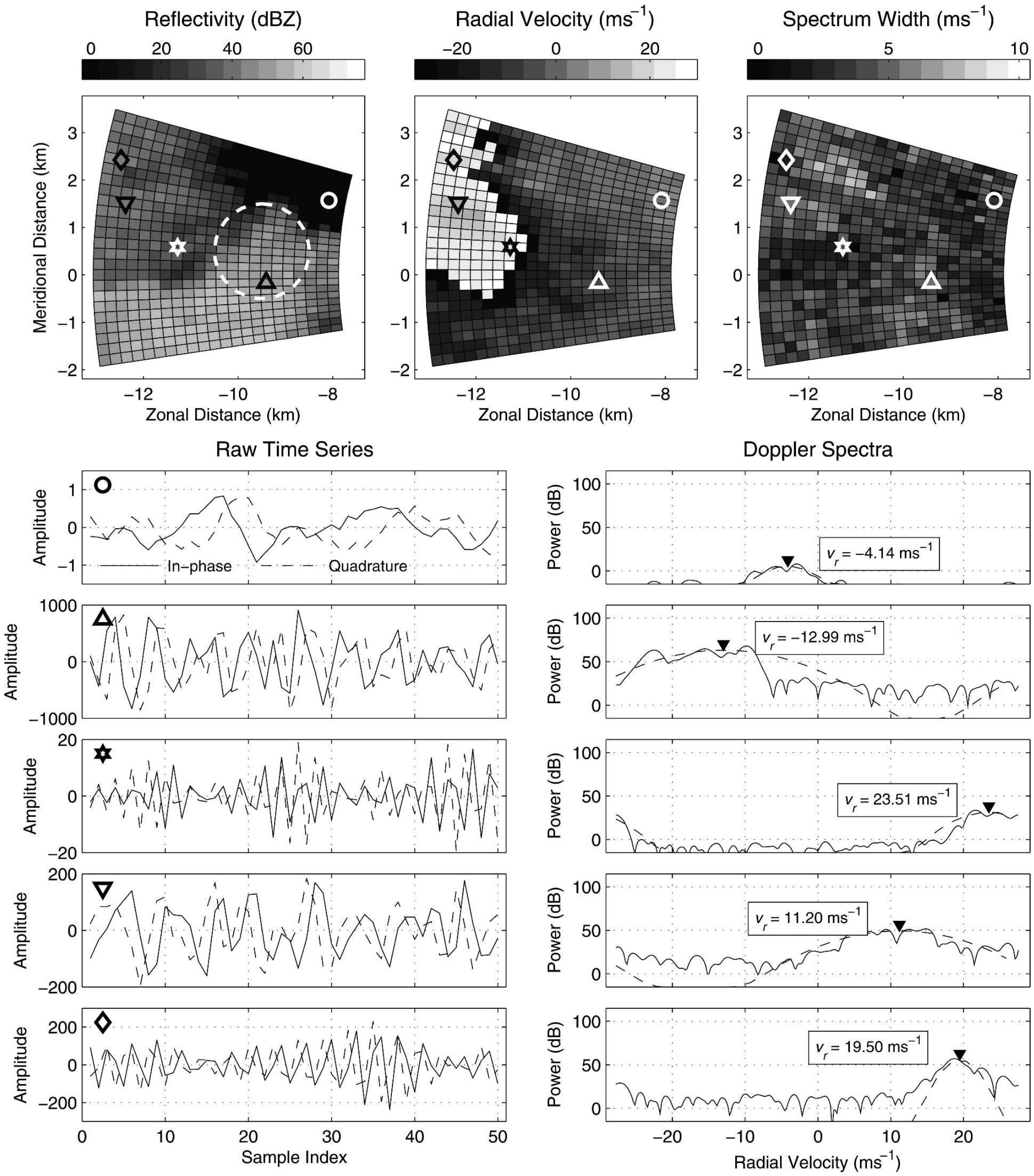

FIG. 5. Example time series and their corresponding Doppler spectra. (top) The three panels show the standard moment maps obtained using covariance processing. (bottom) Five particular examples from the measured fields are provided; (left) the in-phase and quadrature components of the time series, and (right) the Doppler spectra for the corresponding time series. Dashed lines on the spectral plots indicate the resulting Gaussian models from the covariance estimates. The core of the mesocyclone is emphasized with a large dashed circle in upper-left panel.

Using the 93 sets of time series data—one for each receive element—*imaging* or *beam forming* is performed using array processing schemes well established in the atmospheric profiling literature (e.g., Palmer et al. 1998; Cheong et al. 2004b). By adjusting the phase and amplitude for each of the signals, it is possible to produce an *image* of reflectivity, radial velocity, and spectrum width *simultaneously* for each of the desired azimuth angles (Palmer et al. 1998). As such, no beam-smearing results, and temporal evolution in the atmosphere does not distort the estimated fields.

Here, two imaging methods (Fourier and Capon) are compared. The first results were obtained using the standard technique based on Fourier array processing. A Hann window weighting was applied across the array in order to suppress sidelobes in the resulting beam pattern. Estimated fields of reflectivity, radial velocity, and spectrum width are shown in Fig. 7 for a time se-

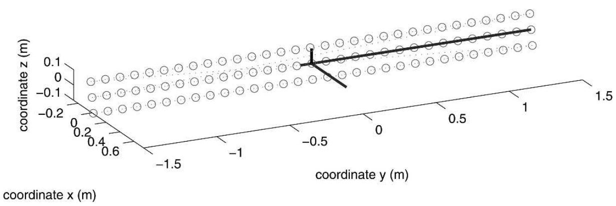

FIG. 6. Simulated 93-element receive array with an element spacing of 10 cm. With a 3-m aperture, the angular resolution at broadside is approximately 1.79°. The imaged domain is 10 km away from the y axis, toward the positive side of the x axis.

quence of 10 scans. Note that the simulated radar is situated to the left of the figure. Each scan was produced from a 120-ms average (120 pulses with a temporal spacing of 5 s). Over this time period, the spatial autocorrelation function was estimated, which is an essential signal-processing step for beam forming (Palmer et al. 1998; Cheong et al. 2004b). The simulated aircraft is seen to progress from the southeast to the northwest of the reflectivity image through the 10-scan sequence. It should be noted that the aircraft echo causes an extreme distortion of the radial velocity and spectrum width estimates. Although the aircraft is essentially a point target, its effect is seen over a large azimuthal swath. Obviously, this is an effect of the sidelobes of the array pattern, even with tapering the array weights. Fourier imaging is plagued by such effects given that the element weights are designed to produce the highest gain in the desired direction but does not taken into account any undesirable signals.

Capon imaging was first used for atmospheric radar applications by Palmer et al. (1998). Over the years, it has proven to be an excellent algorithm for high-resolution studies where clutter mitigation is a concern (e.g., Cheong et al. 2004b). The algorithm is adaptive with the observed data since the array weights are adjusted (scan to scan) in order to minimize interference to the formed beam. In other words, as the beam direction is scanned across the field of view, the element weights (amplitude and phase) are adapted to form nulls in the direction of interference, while keeping a constant gain in the desired direction. The results are evident in Fig. 8, in comparison to Fig. 7, where the aircraft echo is still observed but its adverse effects are limited to only a few closely spaced cells. By adapting the element weights to the observed data, the Capon method is capable of observing nearby weather echoes while nulling point sources, such as the simulated aircraft echo. In addition, it has been shown that the Capon algorithm can increase resolution at only minimal computational expense.

In this section, examples showing the effectiveness of studies of radar signal-processing techniques using the proposed radar simulator have been presented. It should be emphasized that without time series capabilities, which was not the goal of many previous simulators, a thorough investigation of the technical aspects of radar algorithm development would be significantly hindered.

5. Planned near-term improvements

Although many refinements have been added to the radar simulator, mostly in the area of computational complexity, improvements are needed. At present, the radar sampling volume of the simulation domain does not depend on earth curvature or refraction due to spatial variations in refractive index. Of course, these effects are much more important for the long range and do not affect pure signal-processing studies. A simple refinement could be achieved by use of standard equations of beam height, which make use of horizontal homogeneity assumptions and average atmospheric profiles (Rinehart 1997). A more elegant and accurate method would be to essentially track the direction of the beam as it propagates through the simulated atmosphere (Gao et al. 2006; May et al. 2007). In the near future, we intend to implement the latter technique for more accurate measurements but also for studies of refractivity retrieval (Fabry et al. 1997).

Shorter wavelength (such as X band) radars are used for some mobile radar studies and are operationally used in some parts of the world. They have been proposed as *gap-filling* radars for the WSR-88D network, such as those of the National Science Foundation (NFS) Research Center for Collaborative Adaptive Sensing of the Atmosphere (CASA; Brotzge et al. 2005). At these wavelengths, attenuation can significantly affect the measurements leading to biased estimates of rainfall rate, for example. One way to approach this problem for the radar simulator would be to first derive a path-integrated rainwater map, along each radial, given a known radar location relative to the simulated atmosphere. Each scatterer could then be assigned an attenuation factor during the simulation. However, such an approach would be biased by an assumed straight-line propagation path. A better method would be to combine the propagation calculation discussed previously with an attenuation estimate. It would be necessary to update the attenuation coefficient at each time step given advection of the atmosphere.

With the increased interest of polarimetric radar, it is important to consider the possibility of implementing time series polarimetric capabilities on the radar simulator. Fundamentally, two separate time series datasets would be simulated, one for each polarization. Cur-

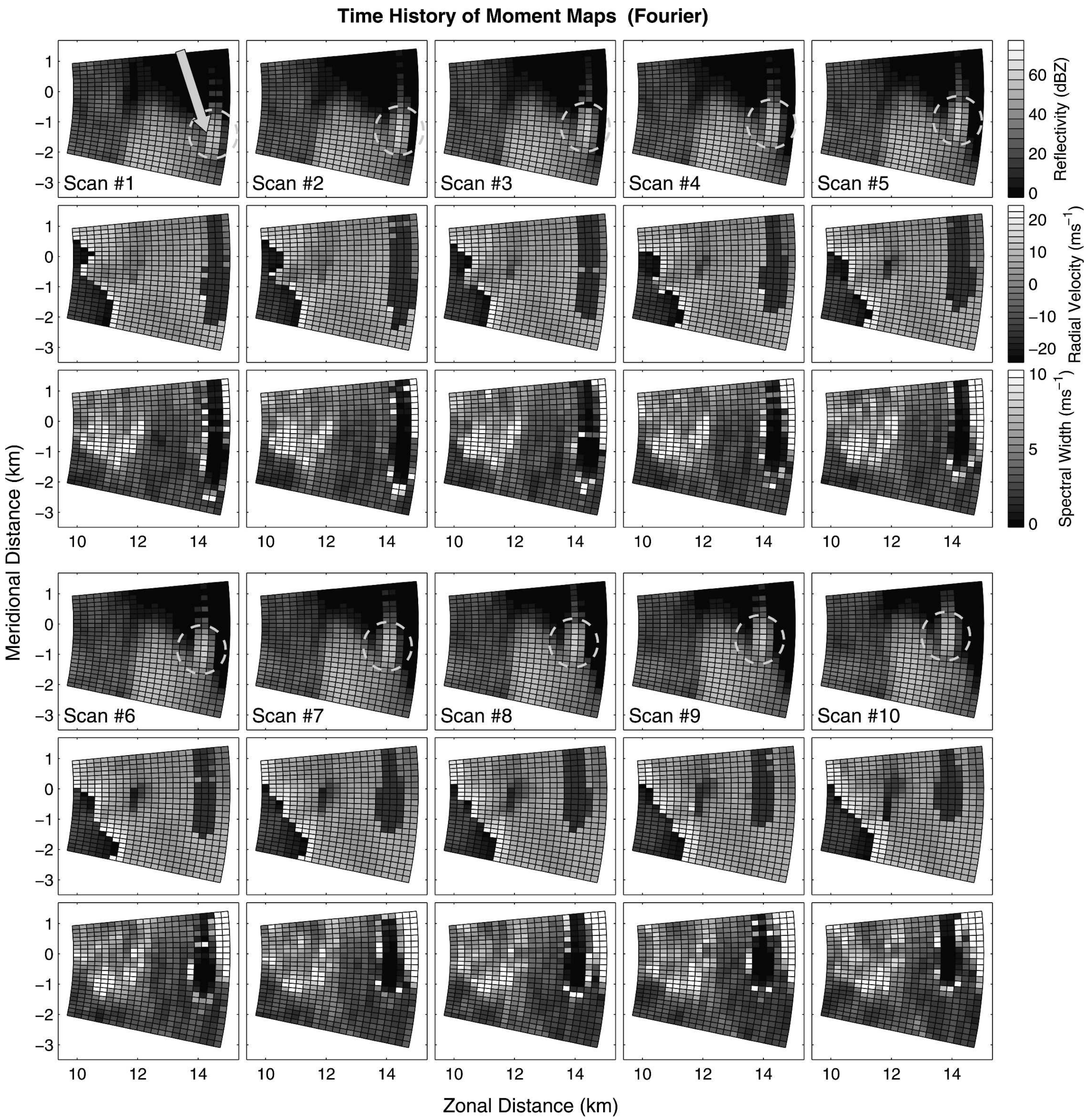

FIG. 7. Standard moment maps obtained using Fourier beam forming and covariance processing. In this simulation, there is an aircraft flying toward the northwest, which can be seen in the processed moment-map sequence. Clutter interference from the aircraft can clearly be seen in this example over a large azimuthal swath.

rently, most of the commonly used single-moment microphysics schemes, as the one used in ARPS, assume Marshall–Palmer drop size distribution for hydrometeors. Although not most realistic, this distribution could be used to *populate* the enclosing volume with a spectrum of drop sizes. It would then be necessary to develop the electromagnetic characteristics (amplitude, phase) for each of these sizes and use these to model the backscattered signal for each polarization. It should also be possible to take advantage of the work of Capsoni et al. (2001) and Jung et al. (2008) for this phase of the planned refinements. In Jung et al. (2008), formulations for various polarimetric parameters, including differential reflectivity and differential phase, are developed for ARPS-based microphysical fields that include ice species.

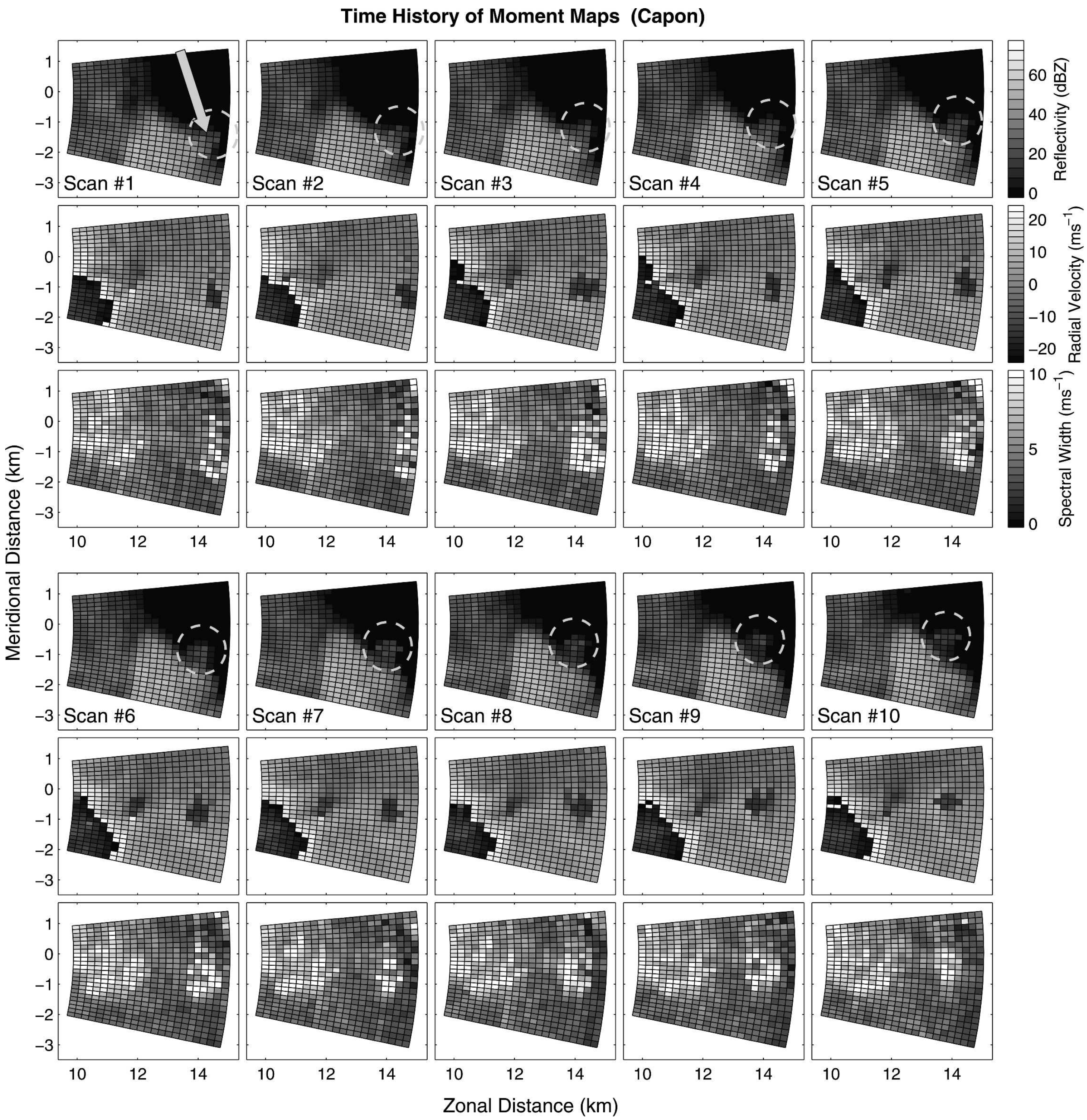

FIG. 8. Same as in Fig. 7, except using the adaptive Capon imaging algorithm. The aircraft echo appears sharper and has little effect on surrounding cells.

6. Conclusions

Based on the previous work of Cheong et al. (2004a), a new weather radar simulator has been proposed that is capable of generating realistic time series data from output from high-resolution numerical weather simulations of precipitating weather systems. To emulate volume scattering (an analog phenomenon), the simulator exploits Monte Carlo integration, which is essentially a random sampling procedure. By populating the model grid or input data volume with thousands of point scatterers, the field of view of the radar is adequately sampled to approximate volume scattering. For computational efficiency, a quad-linear interpolation procedure is used to incorporate the pregenerated atmospheric fields. For this particular application of weather radar, the atmospheric fields were produced from the ARPS model and used to determine the motion of the point scatterers and their reflectivity. Two examples were provided to illustrate the flexibility and capabilities of the simulator. First, a radar system similar to a scanning WSR-88D was investigated. Time series data and their corresponding Doppler spectra were generated for a variety of locations within the data grid. It was evident that realistic radar data were generated. Second, an advanced *imaging* radar was simulated, where a wide transmit beam was used with 93 independent receiving elements. By array processing (beam forming or imaging), it was possible to simultaneously image the radar field of view. Advantages for such phased array systems, in addition to the overall usefulness of the proposed radar simulator, will be investigated in future publications.

Acknowledgments. This work was partially supported by the National Severe Storms Laboratory (NOAA/NSSL) under Cooperative Agreement NA17RJ1227. Ming Xue was also supported by NFS Grants EEC-0313747 and ATM-0530814.

REFERENCES

Anagnostou, E. N., and W. F. Krajewski, 1997: Simulation of radar reflectivity fields: Algorithm formulation and evaluation. *Water Resour. Res.,* **33,** 1419–1428.

Brotzge, J. A., K. Brewster, B. Johnson, B. Philips, M. Preston, D. Westbrook, and M. Zink, 2005: CASA's first test bed: Integrative Project #1. Preprints, *32nd Conf. on Radar Meteorology,* Albuquerque, NM, Amer. Meteor. Soc., 14R.2.

Capsoni, C., and M. D'Amico, 1998: A physically based radar simulator. *J. Atmos. Oceanic Technol.,* **15,** 593–598.

——, ——, and R. Nebuloni, 2001: A multiparameter polarimetric radar simulator. *J. Atmos. Oceanic Technol.,* **18,** 1799–1809.

Caumont, O., and Coauthors, 2006: A radar simulator for high-resolution nonhydrostatic models. *J. Atmos. Oceanic Technol.,* **23,** 1049–1067.

Chandrasekar, V., and V. N. Bringi, 1987: Simulation of radar reflectivity and surface measurements of rainfall. *J. Atmos. Oceanic Technol.,* **4,** 464–478.

Cheong, B. L., M. W. Hoffman, and R. D. Palmer, 2004a: Efficient atmospheric simulation for high-resolution radar imaging applications. *J. Atmos. Oceanic Technol.,* **21,** 374–378.

——, ——, ——, S. J. Frasier, and F. J. López-Dekker, 2004b: Pulse pair beamforming and the effects of reflectivity field variations on imaging radars. *Radio Sci.,* **39,** RS3014, doi:10.1029/2002RS002843.

Doviak, R. J., and D. S. Zrnić, 1993: *Doppler Radar and Weather Observations.* 2nd ed. Academic Press, 562 pp.

Fabry, F., C. Frush, I. Zawadzki, and A. Kilambi, 1997: On the extraction of near-surface index of refraction using radar phase measurements from ground targets. *J. Atmos. Oceanic Technol.,* **14,** 978–987.

Gao, J., K. Brewster, and M. Xue, 2006: A comparison of the radar ray path equations and approximations for use in radar data assimilations. *Adv. Atmos. Sci.,* **23,** 190–198.

Holdsworth, D. A., and I. M. Reid, 1995: A simple model of atmospheric radar backscatter: Description and application to the full correlation analysis of spaced antenna data. *Radio Sci.,* **30,** 1263–1280.

Jung, Y., M. Xue, G. Zhang, and J. Straka, 2008: Assimilation of simulated polarimetric radar data for a convective storm using ensemble Kalman filter. Part I: Observation operators for reflectivity and polarimetric variables. *Mon. Wea. Rev.,* in press.

Krajewski, W. F., R. Raghavan, and V. Chandrasekar, 1993: Physically based simulation of radar rainfall data using a space–time rainfall model. *J. Appl. Meteor.,* **32,** 268–283.

Liu, S., M. Xue, and Q. Xu, 2007: Using wavelet analysis to detect tornadoes from Doppler radar radial-velocity observations. *J. Atmos. Oceanic Technol.,* **24,** 344–359.

Marshall, J. S., and W. M. Palmer, 1948: The distribution of raindrops with size. *J. Meteor.,* **5,** 165–166.

May, R. M., M. I. Biggerstaff, and M. Xue, 2007: A Doppler radar emulator with an application to the detectability of tornadic signatures. *J. Atmos. Oceanic Technol.,* **24,** 1973–1996.

Metropolis, N., and S. Ulam, 1949: The Monte Carlo method. *J. Amer. Stat. Assoc.,* **44,** 335–341.

Palmer, R. D., S. Gopalam, T. Yu, and S. Fukao, 1998: Coherent radar imaging using Capon's method. *Radio Sci.,* **33,** 1585–1598.

Ray, P. S., B. C. Johnson, K. W. Johnson, J. S. Bradberry, J. J. Stephens, K. K. Wagner, and J. B. Klemp, 1981: The morphology of severe tornadic storms on 20 May 1997. *J. Atmos. Sci.,* **38,** 1643–1663.

Rinehart, R. E., 1997: *Radar for Meteorologists.* 3rd ed. Rinehart Publications, 482 pp.

Smith, P. L., Jr., C. G. Myers, and H. D. Orville, 1975: Radar reflectivity factor calculations in numerical cloud models using bulk parameterization of precipitation. *J. Appl. Meteor.,* **14,** 1156–1165.

Stoica, P., and R. Moses, 1997: *Introduction to Spectral Analysis.* Prentice-Hall, 319 pp.

Tong, M., and M. Xue, 2005: Ensemble Kalman filter assimilation of Doppler radar data with a compressible nonhydrostatic model: OSS experiments. *Mon. Wea. Rev.,* **133,** 1789–1807.

Ulbrich, C. W., 1983: Natural variations in the analytical form of raindrop size distribution. *J. Climate Appl. Meteor.,* **22,** 1764–1775.

Xue, M., K. K. Droegemeier, and V. Wong, 2000: The Advanced Regional Prediction System (ARPS)—A multiscale nonhydrostatic atmospheric simulation and prediction tool. Part I: Model dynamics and verification. *Meteor. Atmos. Phys.,* **75,** 161–193.

——, and Coauthors, 2001: The Advanced Regional Prediction System (ARPS)—A multiscale nonhydrostatic atmospheric simulation and prediction tool. Part II: Model physics and applications. *Meteor. Atmos. Phys.,* **76,** 143–165.

——, D.-H. Wang, J.-D. Gao, K. Brewster, and K. K. Droegemeier, 2003: The Advanced Regional Prediction System (ARPS), storm-scale numerical weather prediction and data assimilation. *Meteor. Atmos. Phys.,* **82,** 139–170.

——, S. Liu, and T. Yu, 2007: Variational analysis of oversampled dual-Doppler radial velocity data and application to the analysis of tornado circulations. *J. Atmos. Oceanic Technol.,* **24,** 403–414.

Yu, T.-Y., R. D. Palmer, and D. L. Hysell, 2000: A simulation study of coherent radar imaging. *Radio Sci.,* **35,** 1129–1141.

Zrnić, D. S., 1975: Simulation of weatherlike Doppler spectra and signals. *J. Appl. Meteor.,* **14,** 619–620.